



Article

Thermal Intra-Layer Interaction of Discretized Fractal Exposure Strategies in Non-Isothermal Powder Bed Fusion of Polypropylene

Samuel Schlicht ^{1,2,*}  and Dietmar Drummer ^{1,2}

¹ Institute of Polymer Technology, Friedrich-Alexander-Universität Erlangen-Nürnberg, Am Weichselgarten 10, 91058 Erlangen, Germany

² Collaborative Research Center 814, Friedrich-Alexander-Universität Erlangen-Nürnberg, Am Weichselgarten 10, 91058 Erlangen, Germany

* Correspondence: samuel.schlicht@fau.de

Abstract: Additive manufacturing of material systems sensitive to heat degradation represents an essential prerequisite for the integration of novel functionalized material systems in medical applications, such as the hybrid processing of high-performance thermoplastics and gelling polymers. For enabling an inherent process stability under non-isothermal conditions at reduced ambient temperatures in laser-based additive manufacturing, maintaining a homogeneous layer formation is of vital significance. To minimize crystallization-induced deflections of formed layers while avoiding support structures, the temporal and spatial discretization of the melting process is combined with the subsequent quenching of the polymer melt due to thermal conduction. Based on implementing superposed, phase-shifted fractal curves as the underlying exposure structure, the locally limited temporal and spatial discretization of the exposure process promotes a mesoscale compensation of crystallization shrinkage and thermal distortion, enabling the essential homogeneous layer formation. For improving the understanding of local parameter-dependent thermal intra-layer interactions under non-isothermal processing conditions, geometric boundary conditions of distinct exposure vectors and the underlying laser power are varied. Applying polypropylene as a model material, a significant influence of the spatial distance of fractal exposure structures on the thermal superposition of distinct exposure vectors can be derived, implicitly influencing temporal and temperature-dependent characteristics of the material crystallization and the emerging thermal material exposure. Furthermore, the formation of sub-focus structures can be observed, contributing to the spatial discretization of the layer formation, representing a decisive factor that influences the structure formation and mesoscopic part properties in non-isothermal powder bed fusion of polymers. Consequently, the presented approach represents a foundation for the support-free, accelerated non-isothermal additive manufacturing of both polymers and metals, demonstrating a novel methodology for the mesoscale compensation of thermal shrinkage.

Keywords: non-isothermal; powder bed fusion; polypropylene; low temperature laser sintering; quenching; laser sintering



Citation: Schlicht, S.; Drummer, D. Thermal Intra-Layer Interaction of Discretized Fractal Exposure Strategies in Non-Isothermal Powder Bed Fusion of Polypropylene. *J. Manuf. Mater. Process.* **2023**, *7*, 63. <https://doi.org/10.3390/jmmp7020063>

Academic Editor: Yusheng Shi

Received: 20 February 2023

Revised: 3 March 2023

Accepted: 6 March 2023

Published: 10 March 2023



Copyright: © 2023 by the authors. Licensee MDPI, Basel, Switzerland. This article is an open access article distributed under the terms and conditions of the Creative Commons Attribution (CC BY) license (<https://creativecommons.org/licenses/by/4.0/>).

1. Introduction

Laser-based additive manufacturing processes represent an established technological field for the small series production of load-bearing components. To date, laser-based processing routes are characterized by the application of quasi-isothermal processing, interlinked to inherent limitations in the range of applicable materials and the recyclability [1,2] of unfused material. Considering laser-based additive manufacturing processes, thermal processing conditions are of significant relevance with regard to governing the heating and melting of the powder particles, and ultimately, the solidification kinetics and the microstructural evolution [3] of the resulting part. The interaction between the laser beam and

the powder bed, as well as the thermal history of the material during the process, exhibit a significant impact on the processing stability, associated with exposure-induced residual stresses in LPBF of metal alloys [4,5]. Aforementioned considerations are of significant relevance for the stable layer formation in non-isothermal LPBF of polymers, constituting the physical foundation for the localized meso-scale compensation of material shrinkage. Given the significance of aforementioned thermal intra-layer phenomena and the sensitivity of non-isothermal LPBF of polymers towards thermal processing conditions [3], an enhanced understanding of exposure strategies on emerging thermal processing conditions is essential for enabling support-free LPBF.

In contrast to quasi-isothermal processing, recent developments indicate the possibility for considerably enhancing thermal boundary conditions [3,6], extending the range of material systems applicable for laser-based powder bed fusion (LBPF) of polymers. Previously explored approaches for the non-isothermal powder bed fusion of polymers at reduced ambient temperatures are limited by the use of support structures [7–9] and limited build rates [6], impairing the ecological and economic viability of existing processing routes. To overcome existing limitations in non-isothermal powder bed fusion, the combined spatial and temporal discretization of the crystallization process represents a promising processing strategy for powder-based manufacturing processes. To overcome existing limitations regarding the build rate of non-isothermal processing and for further reducing the thermal exposure of applied materials, a novel methodology based on limiting laser-based material exposure to a spatially discretized dual-step exposure process represents a promising approach. Being associated with the rapid solidification and underlying crystallization kinetics of molten material, the thermal interaction of discrete exposure steps represents a major process influence. With regard to the significance of thermal superposition of consecutively exposed vectors in metal- and polymer-based LPBF processes [4,5,10,11], thermographic investigations allow for the in-depth investigation of process-dependent transient temperature fields, enabling insights into parameter-process interactions and underlying mechanisms in the non-isothermal, support-free LPBF of polymers.

2. State of the Art

2.1. Thermal Processing Conditions in Powder Bed Fusion Processes

The precise control of thermal processing conditions in LPBF of polymers represents the methodological foundation for the established quasi-isothermal LPBF of semi-crystalline polymers. Based on the precise control of thermal boundary conditions, material crystallization is limited to the isothermal crystallization of applied polymers [12–14], allowing for the homogeneous solidification of manufactured components. In contrast, the processing of metal alloys is inherently interlinked to the rapid heating and subsequent solidification of applied materials [15], hence requiring support structures for minimizing solidification-induced deflections. Considering the support-free processing in LPBF of polymers, the local occurrence of non-isothermal processing conditions, associated with an inhomogeneous pre-heating of the powder bed, induces the spatially inhomogeneous crystallization of exposed cross-sections. The emergence of curling is frequently interlinked to build process interruptions, hence impairing the processability of polymer-based material systems with a small thermal processing window [16,17]. Considering an elevated extent of shrinkage of semi-crystalline polymers [18], maintaining inherent advantages of quasi-isothermal LPBF of polymers such as support-free manufacturing while extending the range of applicable polymers indicates the necessity for novel approaches for the additive manufacturing of polymers at reduced ambient temperatures [3,6].

2.2. Process-Structure-Property Interdependencies of Non-Isothermal Additive Processing

Morphological and corresponding mechanical properties of components manufactured by means of quasi-isothermal and non-isothermal laser-based processing show a significant dependency on underlying exposure parameters and temporal process characteristics. Extensive research has been conducted for investigating the influence of exposure

parameters and geometric boundary conditions on emerging thermal process characteristics [11,19] and corresponding mechanical properties [20–22] in quasi-isothermal processing. Parts produced by means of quasi-isothermal LPBF have been found to exhibit a considerable dependency on the consolidation phase, occurring subsequent to the laser-based exposure, exhibiting an influence of the layer time on emerging mechanical properties [23] and on emerging morphological properties [24]. Optically observed consolidation kinetics show a dependency on underlying exposure parameters and rheological material properties [24], implicitly influencing corresponding part densities. Therefore, the influence of varied exposure strategies and emerging temperature fields is associated with the emerging consolidation phase in quasi-isothermal processing. In contrast, the occurrence of a consolidation phase in non-isothermal LPBF [3,6] is inherently restricted due to a considerable supercooling and the corresponding rapid crystallization of the polymer melt [3,6], depending on the emerging cooling rate [25]. Existing research on support-bound LPBF at reduced build chamber temperatures is predominantly based on parameter adaptations of existing linear exposure strategies [7–9,26,27]. To allow for support-free non-isothermal LPBF of polymers, the proposed application of fractally sequenced, locally quasi-simultaneous exposure strategies has been described [3,6], representing the foundation for extending the consolidation phase in non-isothermal processing based on the repetitive exposure of distinct segments. Underlying exposure strategies, applied for the support-free non-isothermal LPBF, rely on the spatial and temporal discretization of the melting and subsequent crystallization of semi-crystalline polymers, demonstrated using polyamide 12 [3,6]. Based on varied quasi-simultaneous exposure times, varying morphological and mechanical properties can be obtained [3], allowing for the local exposure-induced variation of part properties due to altered thermal crystallization conditions. Despite allowing for the exposure-based alteration of emerging part properties, quasi-simultaneous exposure strategies are associated with considerably increased processing times, hence limiting the economic viability of existing non-isothermal processing strategies, indicating the requirement of novel processing strategies in LPBF.

2.3. Crystallization Characteristics of Polypropylene under Non-Isothermal Processing Conditions

High cooling rates, observed in non-isothermal powder bed fusion [3,6], are correlated with considerable supercooling [3] of the polymer melt. Hence, a fundamental understanding of temperature-dependent crystallization rates is required to evaluate the impact of crystallization kinetics on the morphological properties of the formed layers.

A previous study conducted by Mubarak et al. (2001) [28] found a quasi-Gaussian dependency of the crystallization rate of polypropylene on the underlying isothermal crystallization temperature. Rapid cooling rates exceeding 150 K s^{-1} and a crystallization temperature below $85 \text{ }^\circ\text{C}$ predominantly lead to the formation of mesomorphic, metastable states [29]. Considering the glass transition temperature of isotactic polypropylene below 273 K [30], metastable crystalline structures are subject to phase changes at ambient temperatures [31–33], converting into the α -phase while preserving the ductile properties associated with the mesomorphic phase [34,35]. Therefore, given the presence of metastable crystalline structures subsequent to process-inherent quenching, the time-temperature dependence of the thermal and morphological properties of quenched specimens is evident. Furthermore, the cooling-rate dependent formation of varying phase compositions in non-isothermal powder bed fusion embeds implications for the time-dependent formation of material shrinkage due to the repeated thermal exposure in layer-wise manufacturing processes. Hence, a comprehensive understanding of the crystallization kinetics of polypropylene and the resulting morphological changes in non-isothermal powder bed fusion are critical for optimizing the process parameters and achieving desirable part properties.

2.4. Interaction of Processing Parameters and Thermal Process Characteristics

The thermal interaction of consecutively exposed vectors represents a critical factor affecting the emergence of temperature fields in both metal-based [4,5,36] and polymer-

based [11,19] powder bed fusion. Given the predominant use of linear exposure strategies in LPBF, the accumulation of thermal energy resulting from the thermal superposition of consecutively exposed vectors has been found to significantly influence the formation of thermal stresses [37] and melt pool geometries [10]. Additionally, the thermal interaction of consecutively exposed vectors is considerably affected by the scan vector length, which implicitly affects the time span of intermediate cooling prior to the repeated heating by the laser beam.

The significance of the scan vector length was demonstrated with regard to elevated melt pool temperatures arising from reduced vector lengths [11] in LPBF of polyamide 12. Furthermore, a negative correlation of residual stresses and the underlying vector length has been derived [38,39], leading to the development of segmented exposure strategies, extensively applied in LPBF of alloys prone to hot cracking. In contrast to linear exposure strategies, non-linear fractal exposure strategies have been shown to minimize hot cracking in LPBF of nickel-based alloys [40]. Furthermore, fractal exposure strategies allow for reducing the influence of the exposed geometry on emerging peak temperatures due to inherent scale-invariant structures [41]. In addition, the use of scale-invariant, self-similar exposure strategies allows for reducing the effect of heat accumulation despite significantly reduced vector lengths [41], indicating their improved applicability for spatially discretized exposure strategies.

3. Materials and Methods

3.1. Implementation of Discretized Exposure Strategies

For obtaining a process-inherent spatial and temporal discretization of the formation and subsequent crystallization [6] of distinct exposure vectors, fractal, space-filling, and self-similar curves, commonly referred to as FASS-Curves [42], are applied in the form of the Peano curve [43]. The applied exposure structure is characterized by an equidistant alignment of the exposed vectors, yielding a homogeneous energy input into the powder bed on a mesoscopic scale. By applying increased hatch distances, the formation of interconnected melt pools is inherently minimized, promoting a discrete crystallization of distinct exposed vectors. The exposure process is divided into two consecutive exposure steps, compromising a superposition of identical exposure structures. For achieving an optimized layer homogeneity, a biaxial displacement, referred to as phase shift corresponding to 50% of the underlying hatch distance, is specified, promoting the aforementioned discretized crystallization of consecutively exposed vectors. The interdependence of the specified hatch distance and the corresponding exposure structure is displayed in Figure 1.

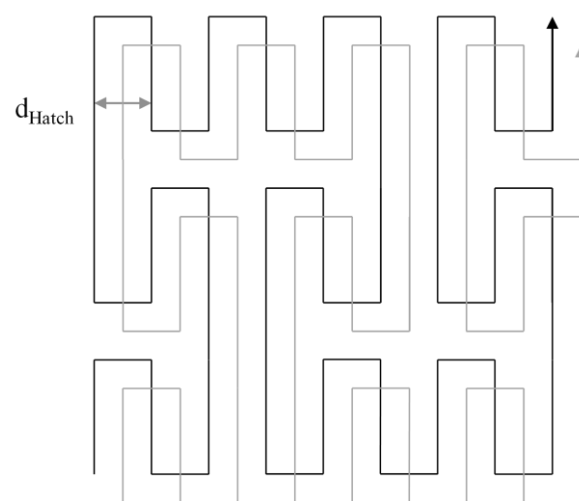


Figure 1. Schematic depiction of the local structure of superposed, fractal exposure structures based on the space-filling Peano curve.

Relying on scale-invariant properties of the applied space-filling curve, locally identical exposure structures are obtained, allowing for the predominant invariance of resulting local, transient temperature fields towards varying exposed cross-sections. Based on the implementation of a dual-step exposure, the aforementioned geometric invariance is limited by the inherent time offset of the exposure of consecutive exposure steps, yielding a temporal discretization in addition to the inherent spatial discretization.

3.2. Exposure Implementation and Applied Materials

The preparation of fractal, discretized exposure strategies, specified in chapter 3.1., is conducted by means of iterative programming, implemented in Python 3.9., allowing for specifying scale-invariant geometric features of the space-filling curve. Resulting geometric structures are implemented using a freely configurable LPBF research system, previously described by Drummer et al. (2019) [12], allowing for highly dynamic beam deflection. Based on the applied optical setup comprising a carbon dioxide laser of type Coherent Diamond C-55 (Coherent, Inc., Santa Clara, USA) and a f-Theta lens, a focal diameter ($I = 1/e^2$) of 0.5 mm is obtained, exhibiting a Gaussian intensity distribution.

Commercially available polypropylene powder of type Ultrasint® PP 1400 (BASF SE, Ludwigshafen, Germany) is applied as the underlying material, exhibiting a melting peak of $T_m = 137.2 \text{ °C} \pm 0.29$, derived by means of differential scanning calorimetry ($dT/dt = 10 \text{ K min}^{-1}$), and a viscosity number (ISO 1628-3 [44]) of $207.7 \text{ mL g}^{-1} \pm 1.7$. The used material is characterized by irregular, partly aspherical particles, displayed in Figure 2, associated with cryogenic milling of the feedstock material. The applied feedstock exhibits a mean particle diameter of $d_{50} = 62.39 \text{ }\mu\text{m} \pm 2.42$.

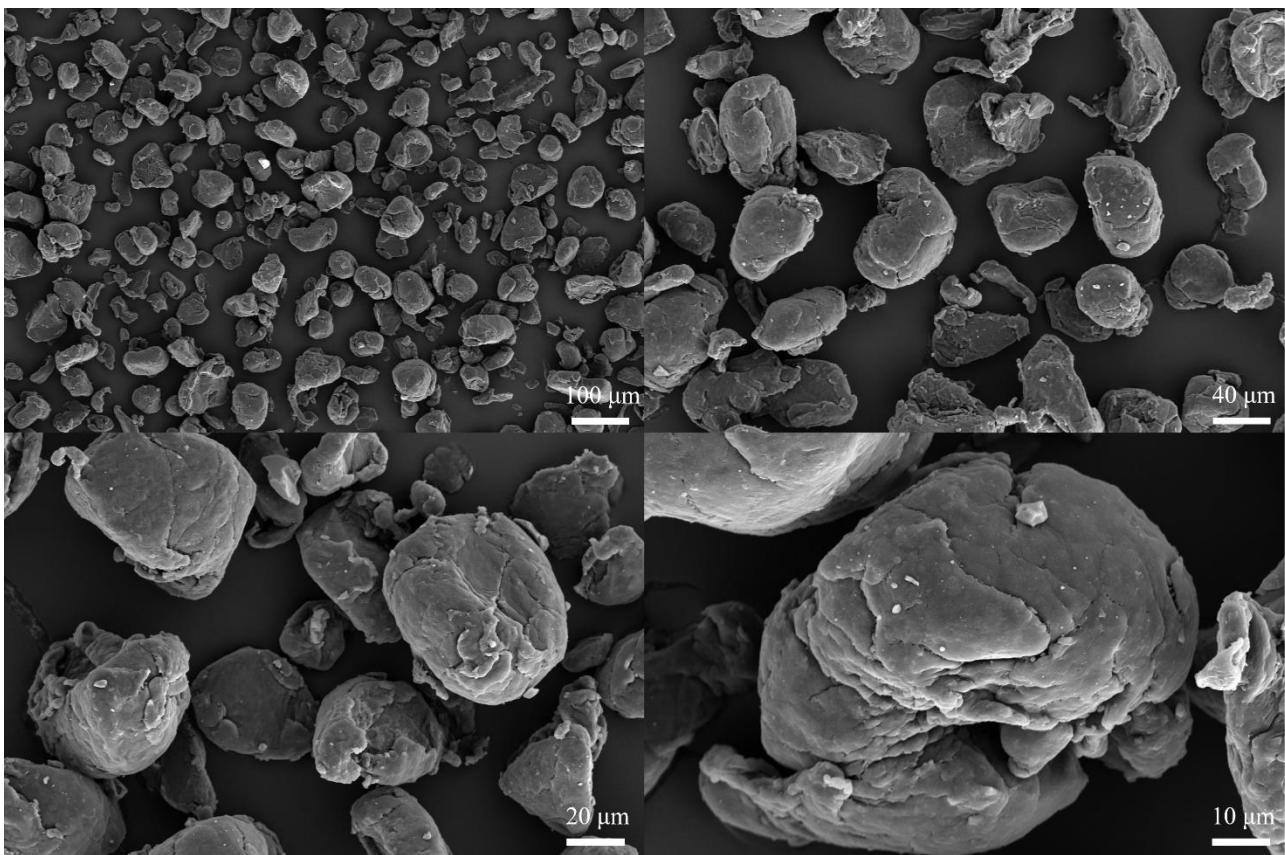


Figure 2. Scanning electron micrographs of the applied polypropylene powder.

For optimizing rheological powder properties, the material is modified by means of rotational dry blending, adding a fraction of 0.1% of fumed silica (Aerosil R 8200, Evonik Industries AG, Essen, Germany), yielding a bulk density of $0.337 \text{ g cm}^{-3} \pm 0.0039$.

3.3. Design of Experiments

For investigating interactions of varied geometric boundary conditions of the applied exposure structure and corresponding exposure parameters, the hatch distance of distinct, consecutively exposed scan vectors and the laser power are varied in discrete steps. The resulting two-factorial parameter variation is displayed in Table 1.

Table 1. Overview of applied processing parameters.

Parameter Set/-	Hatch Distance/mm	Laser Power/W	Part Edge Length/mm
1	0.3	11.00	22.5
2		12.25	
3		13.50	
4		14.75	
5		16.00	
6	0.4	11.00	30
7		12.25	
8		13.50	
9		14.75	
10		16.00	
11	0.5	11.00	37.5
12		12.25	
13		13.50	
14		14.75	
15		16.00	

Further constant boundary conditions include an exposure speed of $v = 1500 \text{ mm s}^{-1}$ and a powder bed temperature of $T_B = 25 \text{ }^\circ\text{C}$, corresponding to the ambient temperature. Derived process characteristics, that are based on thermographic investigations, are described in the following section.

3.4. Thermographic In Situ Investigations

Thermal imaging, applied for in situ assessment of emerging thermal fields and emerging process-dependent crystallization kinetics, is based on integrating an infrared camera of type IRCAM VELOX 1310k SM (IRCAM GmbH, Erlangen, Germany) into the build chamber. Based on the thermographic measurement setup, an isotropic resolution of $140 \times 140 \text{ } \mu\text{m}^2$ and a frame rate of 355 Hz are obtained. A sapphire window is employed for avoiding measurement errors due to scattered laser radiation. Based on preceding thermal calibrations, an emission coefficient of $\epsilon = 0.805$ is applied for deriving thermal process characteristics. To obtain parameter-dependent cooling rates, the time derivative is derived over a time span of 250 ms for minimizing the influence of measurement noise. In addition, based on analytical investigations of the temporal variability of derived cooling rates, the exothermal material crystallization is characterized. For deriving the temporal maximum of observed cooling rates, a 5th degree polynomial fit is applied for minimizing the influence of measurement noise on the determined crystallization peak temperature.

3.5. Topological and Thermal Part Characterizations

For assessing topological properties of the layer formation, scanning electron microscopy (SEM) is applied, using a scanning electron microscope of type Zeiss Gemini (Carl Zeiss Microscopy GmbH, Oberkochen, Germany). Thermal part properties are characterized by applying differential scanning calorimetry, using a device of type DSC 2500 (TA Instruments, New Castle, DE, USA). A heating rate of $dT/dt = 60 \text{ K min}^{-1}$ is applied for optimizing the sensitivity of the measurement towards minor effects such as the occurrence of cold crystallization.

4. Results and Discussion

4.1. Spatial Exposure Discretization

Applied exposure strategies are characterized by a structural geometry-invariance, corresponding to the structure of the underlying space-filling curve. Based on thermographic investigations, a segment-wise occurrence of peak temperatures can be identified, being associated with heat accumulation being limited to the first iteration of the fractal curve, displayed in Figure 3.

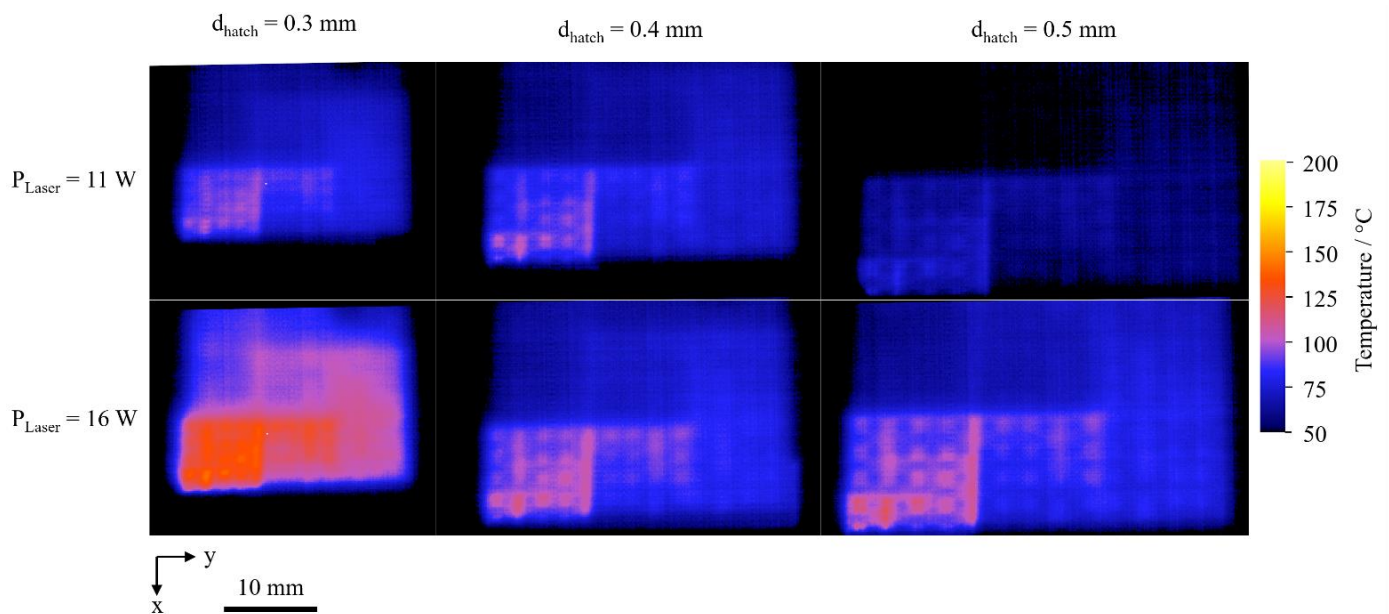


Figure 3. Observed temperature fields during the second exposure step in dependence on the applied laser power and the underlying hatch distance, $T_B = 25 \text{ }^\circ\text{C}$, $\varepsilon = 0.805$.

Observed spatial distributions indicate a considerable influence of the thermal vector–vector interaction on the resulting thermal history. An increase of applied hatch distances is correlated with a more pronounced spatial separation and resulting discretization of formed local heat build-ups. Formed temperature fields are characterized by the short-term formation of local heat spots exceeding the melting temperature, separated by sections that did not exceed the melting peak temperature, located between distinct exposure vectors. The implicit discretization is assumed to represent an inherent prerequisite to non-isothermal layer formation, implying the significance of thermal intra-layer interactions on the processing stability.

4.2. Process-Dependent Thermal Vector–Vector Interaction

The influence of thermal interactions of consecutively exposed vectors can be observed with regard to emerging peak temperatures, resulting cooling conditions, as well as in situ assessed crystallization kinetics and corresponding crystallization peak temperatures. The observed negative correlation of the underlying hatch distance and emerging thermographically observed peak temperatures is associated with a thermal superposition of

consecutive scans, previously described to considerably influence emerging temperature fields in quasi-isothermal processing [11].

Displayed in Figure 4, thermographically observed time–temperature profiles display a considerable influence of the applied laser power and the underlying hatch distance. Thermographic observations indicate a stepwise, non-linear time–temperature profile, being associated with a stepwise temperature increase induced by a thermal superposition of consecutively exposed vectors. A step-wise temperature increase can be observed regardless of the applied hatch distance, indicating an influence of thermal superposition of consecutively exposed vectors on emerging peak temperatures. Observed peak temperatures are limited by the applied measurement frame rate of 355 Hz and the limited spatial resolution, limiting the detection of occurring peak temperatures due to the rapid subsequent cooling and the spatially limited heating.

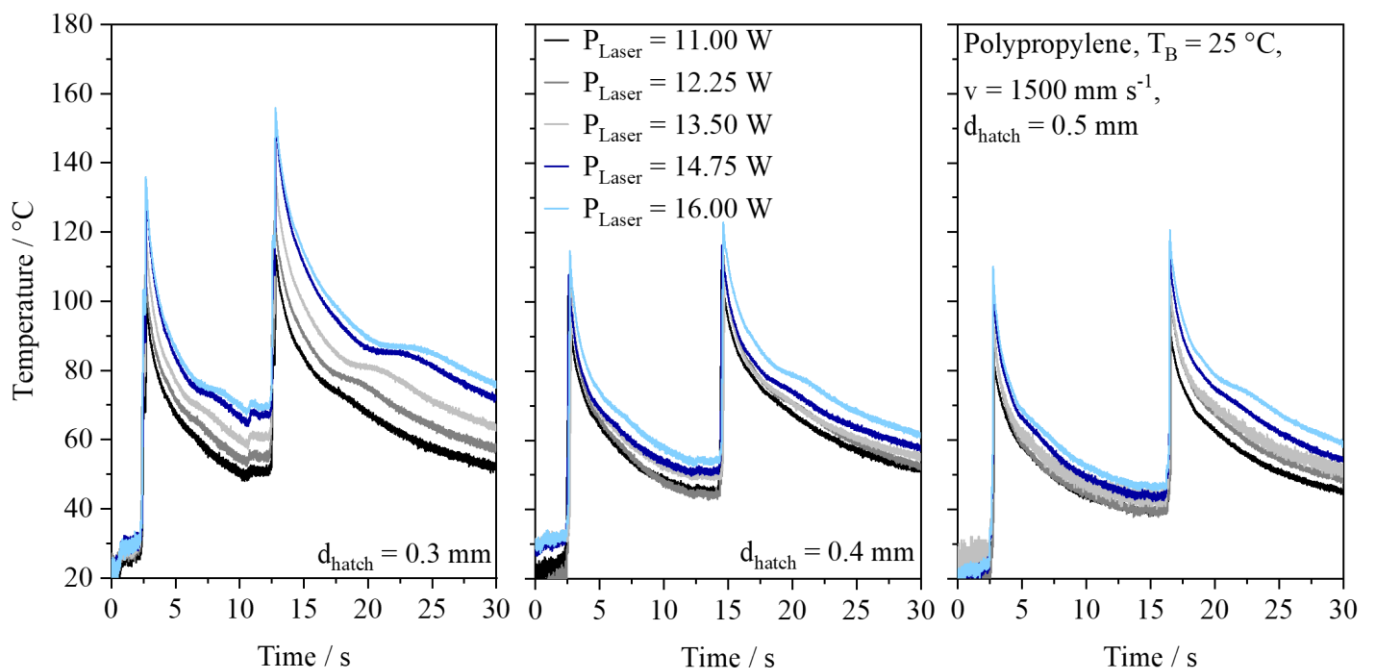


Figure 4. Influence of hatch distance and laser power on emerging time–temperature profiles, $v_{\text{Exposure}} = 1500 \text{ mm s}^{-1}$.

Based on the high cooling rates observed in non-isothermal processing, exothermic material crystallization can be distinguished from random noise based on the formed temporal peak of the cooling rate [3], allowing for detecting characteristic temporal variations in the derived cooling rate. To minimize the influence of process noise on the derived peak crystallization temperature, a polynomial fit is applied, displayed in Figure 5.

The influence of the crystallization process on emerging temperature fields in quasi-isothermal powder bed fusion of polymers has been previously described based on numerical approaches [45]; however, the thermographic observation of the influence of the cooling process is limited to non-isothermal processing due to the rapid crystallization and the temporal contraction of the crystallization process. Elevated energy density levels, correlated with increased processing peak temperatures, exhibit a positive correlation with corresponding crystallization temperatures. Based on the time- and intensity-dependent formation of temperature fields [21], observed varying crystallization kinetics are assumed to rely on exposure-induced variations of transient thermal boundary conditions. The influence of the dual-step exposure process and varied processing conditions on emerging crystallization peak temperatures is displayed in Figure 6. Observed crystallization temperatures indicate a positive correlation with the applied energy density, implicitly influenced by the laser power and the underlying hatch distance. In addition, the initial exposure

cycle is characterized by significantly reduced crystallization temperatures, correlated with previously discussed reduced peak melt pool temperatures.

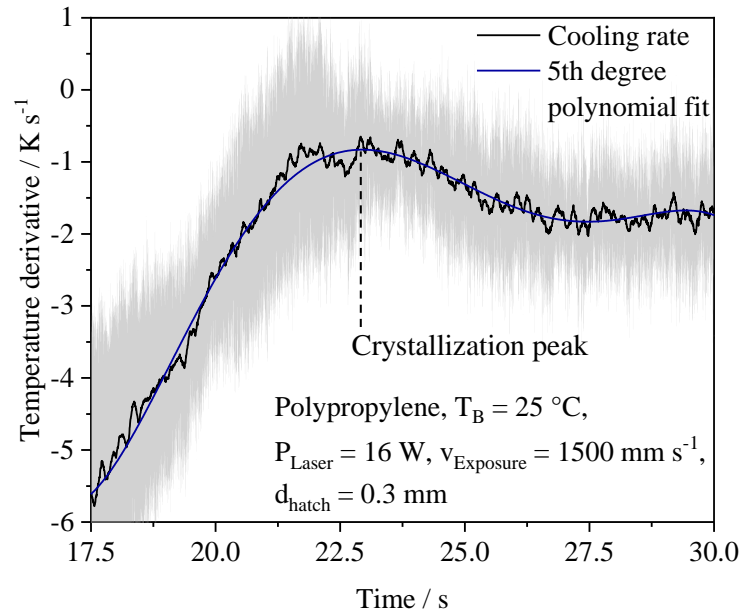


Figure 5. Exemplary depiction of the determination of thermographically represented material crystallization based on the temporal derivative of observed cooling rates.

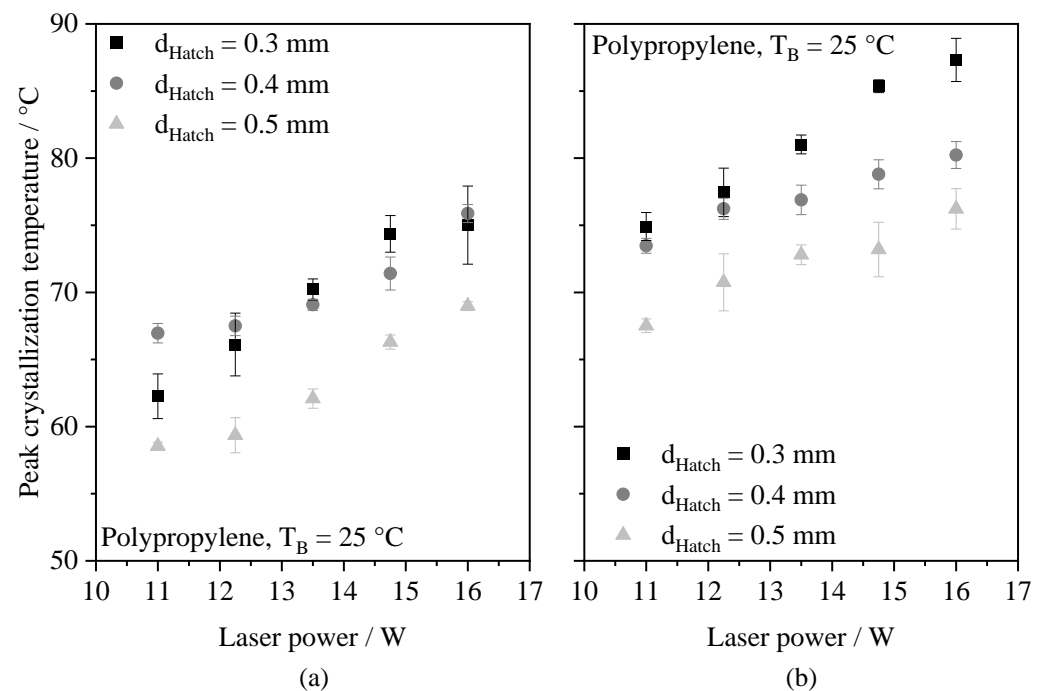


Figure 6. Influence of varying processing parameters on corresponding peak crystallization temperatures observed during the initial (a) and the second (b) exposure cycle.

Furthermore, the applied hatch distance exhibits a significant influence on the sensitivity of emerging crystallization temperatures to the applied laser power. Therefore, the inherent thermal superposition implies the significance of fractal exposure strategies for obtaining locally geometry-invariant temperature fields. In addition, a reduced hatch distance, associated with a more pronounced thermal superposition of consecutively exposed vectors, is correlated with an increase of corresponding crystallization temperatures

during the second exposure step. Adapted thermal process properties are assumed to rely on the influence of a partially consolidated layer, leading to an increased efficiency of the laser-material interaction due to a predominantly superficial laser absorption. The laser-powder interaction has been described to show a dependency on the powder bed topology [46], hence influencing the spatial heat distribution formed during the initial exposure cycle, promoting reduced superficial temperatures.

The observed interdependence of thermographically determined crystallization temperatures and underlying processing parameters is correlated with resulting process-induced transient cooling rates, showing a positive correlation of the applied laser power and the peak cooling rate. In situ determined cooling rates and corresponding crystallization temperatures show an accordance with ex situ observed relations of the crystallization time and the underlying cooling rate, described by Mileva et al. (2020) [47].

Corresponding transient cooling rates, displayed in Figure 7, are significantly influenced by the underlying exposure cycle and the applied hatch distance, hence determining the peak cooling rate. Furthermore, the hatch distance can be identified as a decisive factor determining the extent of the influence of the varied laser power on emerging cooling rates. A reduced hatch distance of $d_{\text{hatch}} = 0.3 \text{ mm}$ is associated with an increased variance of observed cooling rates. In addition, the effect of the underlying laser power on the peak cooling rate is correlated with the applied hatch distance. The identified interaction of the hatch distance and the applied laser power is attributed to the enhanced thermal interaction of distinct exposure paths.

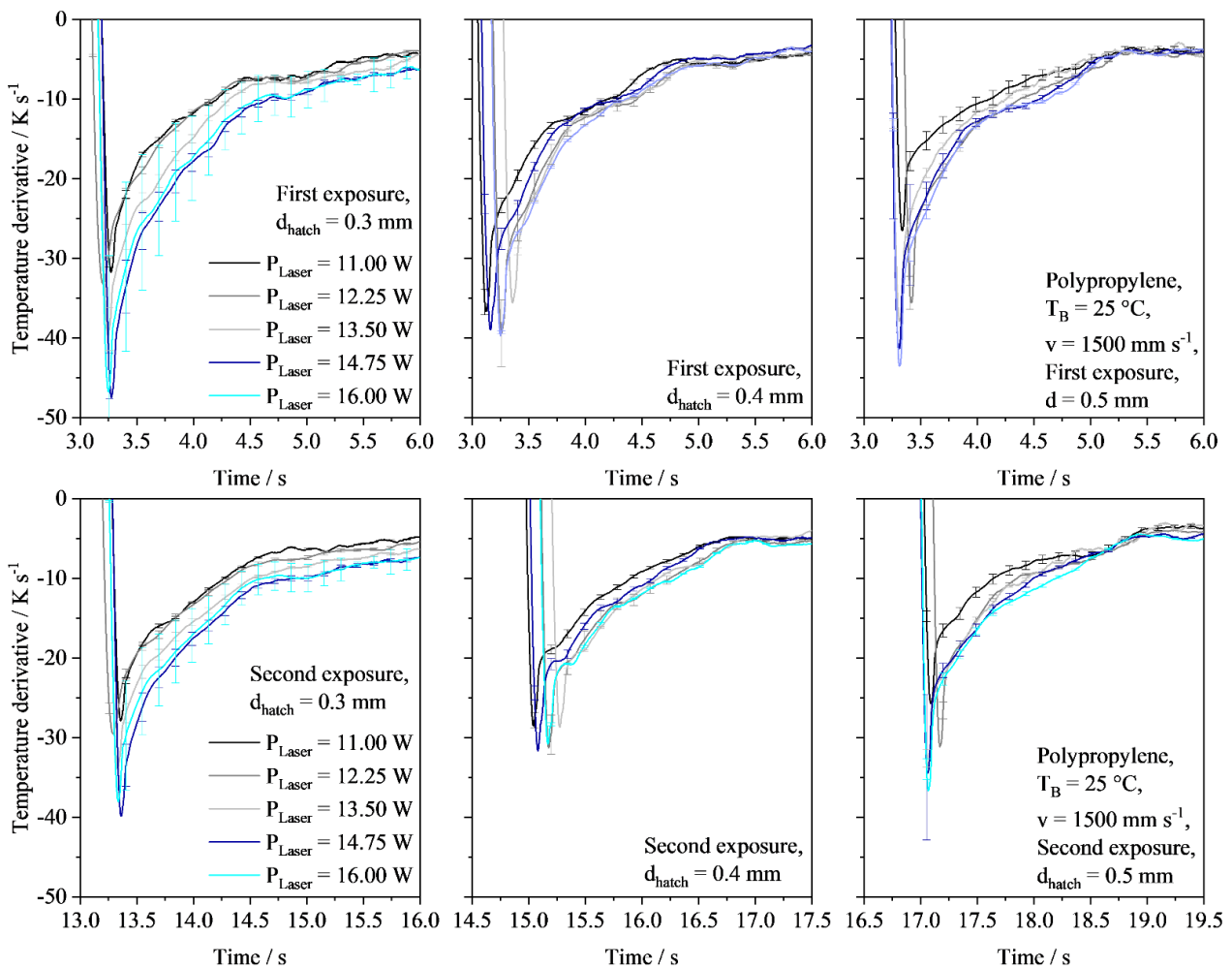


Figure 7. Influence of varied process parameters and geometric boundary conditions on resulting transient cooling rates.

Considering an increased extent of heat accumulation [5,10] due to the reduced hatch distance, observed peak cooling rates are interlinked to elevated peak temperatures. In contrast, the relation of elevated cooling rates and increased peak temperatures does not apply to subsequent exposure cycles. Despite considerably increased peak temperatures observed during the second exposure cycle, corresponding cooling rates depict considerably lower peak values. Therefore, elevated peak crystallization temperatures observed during the second exposure cycle are associated with underlying reduced cooling rates despite overall elevated peak processing temperatures, indicating a decoupling of the peak temperature and subsequent cooling rates occurring during the second exposure cycle. Based on thermographic observations, a crystallization half time exceeding 1000 ms can be observed, inconsistent with flash scanning calorimetric observations [47], indicating significantly increased crystallization half times. This apparent contradiction is assumed to rely on a temporal distribution of the crystallization process, being associated with a temperature gradient oriented perpendicular to the powder bed, considerably influencing the initiation time of the crystallization process. In contrast to the processing of polyamide 12 [3], the crystallization of polypropylene is observed to occur at reduced cooling rates, displaying temporal cooling rates of less than 10 K s^{-1} during the crystallization process. This divergence is likely associated with reduced peak processing temperatures and overall reduced cooling rates due to a reduced temperature difference between the build chamber temperature and the quasi-isothermal crystallization temperature.

Despite the thermal superposition of consecutively exposed vectors, an intermediate discretization of formed thermal fields can be observed, indicating an influence of the applied Gaussian intensity distribution on the resulting discretization. Considering a laser spot diameter of $d_{\text{Focus}} = 0.5 \text{ mm}$ ($I = 1/e^2$), a discretization of sub-focus hatch distances, e.g., of applied hatch distances of 0.3 mm and 0.4 mm, is based on a reduced focused intensity in the edge region of a specific exposed vector, contributing to the stable layer formation. The underlying mechanism of the spatial discretization of distinct vectors is schematically displayed in Figure 8.

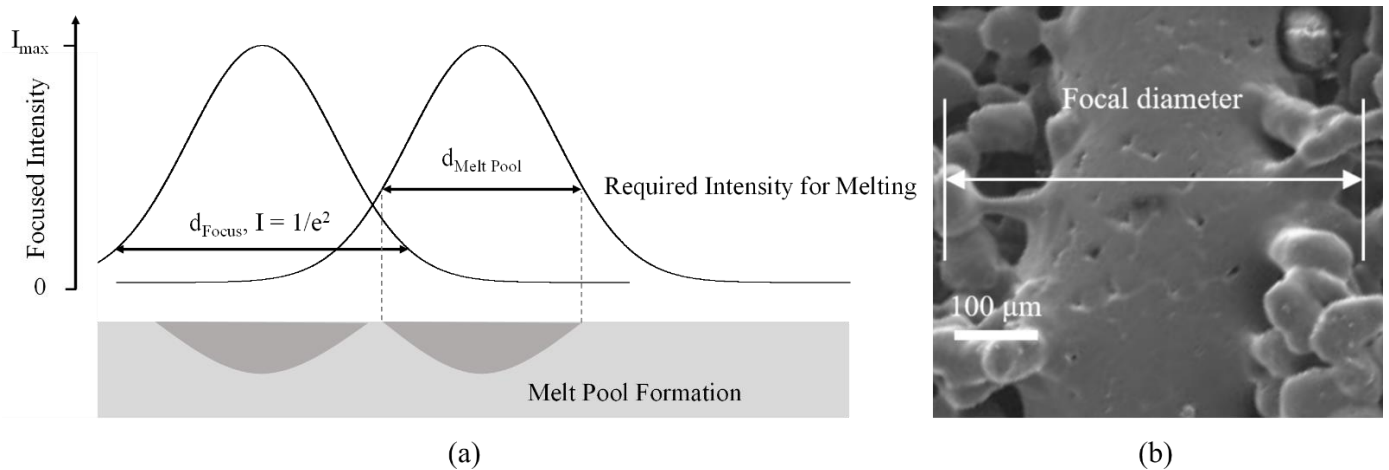


Figure 8. (a) Schematic depiction of the influence of the Gaussian laser intensity distribution on the intensity-dependent discretization of distinct melt pools during the initial exposure step; and (b) corresponding exemplary scanning electron micrographs, depicting the sub-focus formation of recrystallized melt pools and nearby adhering powder particles during the initial exposure cycle, $P_{\text{Laser}} = 16 \text{ W}$.

Given the influence of the peak focused intensity on the resulting melt pool width, an interaction of the applied laser power and the spatial discretization is evident, hence limiting the applicable focused intensity. However, in addition to the spatial discretization of distinct vectors, the temporal discretization further contributes to the discretized crystallization of distinct paths. An increased time shift between the exposure of vectors

next to each other is assumed to avoid the inherent heat build-up [4,5] and to promote the rapid cooling of distinct vectors, contributing to a spatially discrete crystallization. In contrast, previously discussed thermographic observations corroborate a contribution of reduced hatch distances to the thermal superposition of vectors next to each other, hence slowing the cooling process, potentially leading to larger melt pools. Therefore, the spatial and the temporal discretization are assumed to synergistically contribute to the discretized crystallization of consecutively exposed vectors, allowing for the mesoscale compensation of thermal- and crystallization-induced shrinkage.

These observations indicate an intermediate discretization of exposed exposure paths, followed by the exposure-induced bonding of previously unconnected recrystallized melt pools. Therefore, the observed thermal interaction of distinct exposure vectors located next to each other does not exhibit a direct correlation with the process-inherent requirement of the discretization of the melt pool formation. However, a reduction of underlying hatch distances combined with a sufficiently high laser intensity may inhibit the aforementioned spatial discretization of the melting process [6], highlighting the significance of a holistic optimization of the geometric exposure structure and underlying exposure parameters.

4.3. Process-Dependent Thermal Part Properties

Based on thermal part properties, process-specific part characteristics can be derived. With regard to the influence of processing conditions on emerging melting peak temperatures, structural influences and interactions of the applied laser power and the underlying hatch distance can be derived, displayed in Figure 9.

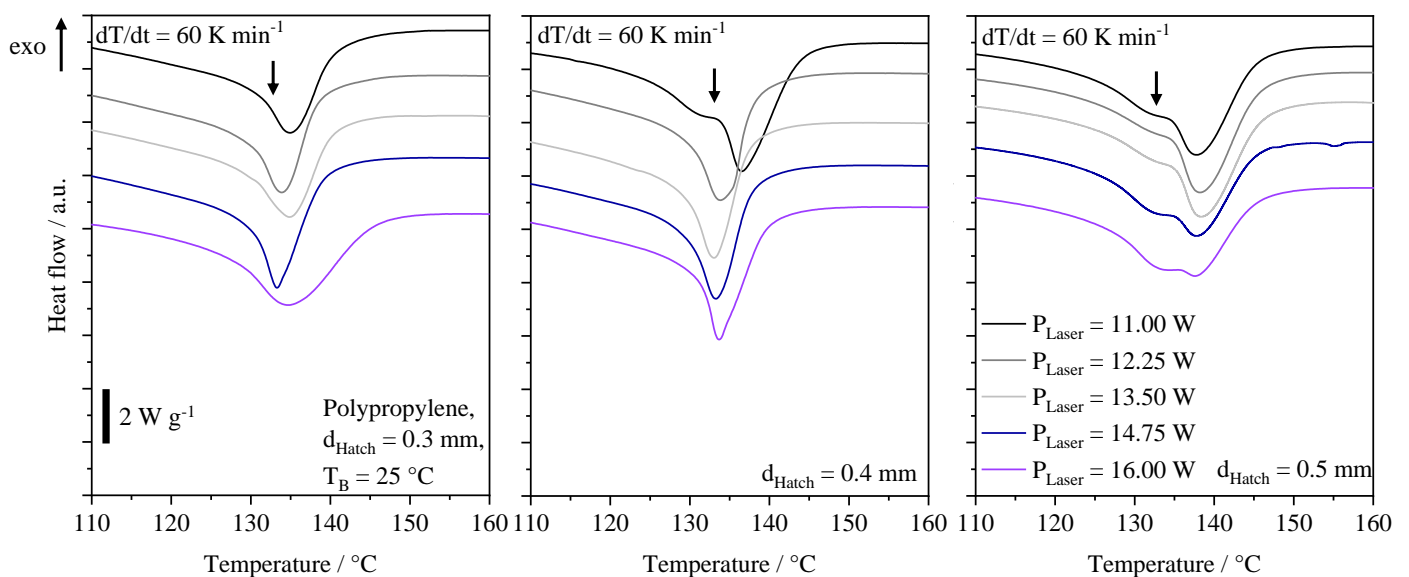


Figure 9. Differential calorimetric part properties in dependence on underlying spatial and scalar process properties; melting peak of recrystallized material indicated by black arrow.

Given a sufficient degree of melting, a melting peak temperature below 135 °C can be identified, associated with the process-induced recrystallization. In contrast, an elevated hatch distance of 0.5 mm leads to an insufficient extent of melting, correlated with an increased melting peak temperature exceeding 137 °C, corresponding to unaffected feedstock material. Therefore, an increase of the applied laser power is associated with broadened melting peaks, partially depicting a distinct double peak, corresponding to a superposition of virgin and processed material. Consequently, thermal part properties depict an accordance with thermographically observed peak temperatures and corresponding crystallization peaks, indicating a partly insufficient melting. Furthermore, the applied hatch distance can be identified as a decisive factor for resulting thermal part properties due

to the thermal superposition of consecutively exposed vectors, considerably influencing the laser power required for complete melting.

5. Conclusions and Outlook

Within the present study, the interaction of the spatial discretization of consecutive exposure vectors and the applied laser intensity were investigated with regard to the thermal interactions of vectors next to each other as well as with regard to influences on the layer formation. By applying the fractal Peano curve as the underlying exposure structure, the locally discretized melting and crystallization of polypropylene could be observed. The fractal exposure structure is associated with the implicit mesoscale compensation of material shrinkage, allowing for the controlled crystallization and the avoidance of solidification-related part deflections.

Based on thermographic investigations, a significant negative correlation of the spatial distance of distinct vectors and the corresponding thermal superposition, leading to heat accumulation, could be observed. Increased hatch distances, associated with the discretized crystallization and the inherent compensation of crystallization shrinkage, lead to a significant reduction of in situ assessed crystallization peak temperatures. In contrast, a reduction of applied hatch distances as well as the application of increased laser power levels is associated with an increased thermal superposition, leading to a slowed cooling process and the corresponding emergence of increased crystallization temperatures. Although the thermal superposition of distinct scan vectors considerably influences emerging thermal process characteristics, the thermal vector–vector interaction does not exhibit a direct correlation with mechanical bonding of molten segments next to each other, being associated with the applied Gaussian intensity distribution of the laser focus. Corresponding microscopic observations provide indications that the observed discretization, occurring for the application of sub-focus hatch distances, is interlinked to the intermediate formation of sub-focus melt pools, enabling a mechanical discretization despite a considerable extent of thermal vector–vector interaction. Consequently, time-dependent as well as spatial process characteristics represent essential prerequisites for enabling minimized residual stresses in powder bed fusion processes, allowing for support-free additive manufacturing.

Future research will focus on the holistic optimization of the layer formation with regard to quantifying the mutual interaction of time-dependent and spatial influences on emerging microstructural properties. Furthermore, discretized powder bed fusion processes embed promising implications for potential applications for the processing of materials sensitive to heat degradation and in powder bed fusion of metallic materials and metal matrix composites.

Author Contributions: Conceptualization, methodology, software, validation, investigation, writing—original draft preparation, S.S.; Supervision, project administration, funding acquisition, D.D. All authors have read and agreed to the published version of the manuscript.

Funding: Funded by the Deutsche Forschungsgemeinschaft (DFG, German Research Foundation) Project-ID 61375930 SFB 814—“Additive Manufacturing”, sub-project B03. We acknowledge financial support by Deutsche Forschungsgemeinschaft and Friedrich-Alexander-Universität Erlangen-Nürnberg within the funding program “Open Access Publication Funding”.

Data Availability Statement: The data presented in this study are not publicly available due to ongoing research in this field.

Conflicts of Interest: The authors declare no conflict of interest.

References

1. Paolucci, F.; van Mook, M.J.H.; Govaert, L.E.; Peters, G.W.M. Influence of post-condensation on the crystallization kinetics of PA12: From virgin to reused powder. *Polymer* **2019**, *175*, 161–170. [[CrossRef](#)]
2. Wudy, K.; Drummer, D. Aging effects of polyamide 12 in selective laser sintering: Molecular weight distribution and thermal properties. *Addit. Manuf.* **2019**, *25*, 1–9. [[CrossRef](#)]

3. Schlicht, S.; Cholewa, S.; Drummer, D. Process-Structure-Property Interdependencies in Non-Isothermal Powder Bed Fusion of Polyamide 12. *J. Manuf. Mater. Process.* **2023**, *7*, 33. [[CrossRef](#)]
4. Li, Y.; Gu, D. Thermal behavior during selective laser melting of commercially pure titanium powder: Numerical simulation and experimental study. *Addit. Manuf.* **2014**, *1–4*, 99–109. [[CrossRef](#)]
5. Shi, Q.; Gu, D.; Xia, M.; Cao, S.; Rong, T. Effects of laser processing parameters on thermal behavior and melting/solidification mechanism during selective laser melting of TiC/Inconel 718 composites. *Opt. Laser Technol.* **2016**, *84*, 9–22. [[CrossRef](#)]
6. Schlicht, S.; Greiner, S.; Drummer, D. Low Temperature Powder Bed Fusion of Polymers by Means of Fractal Quasi-Simultaneous Exposure Strategies. *Polymers* **2022**, *14*, 1428. [[CrossRef](#)] [[PubMed](#)]
7. Niino, T.; Haraguchi, H.; Itagaki, Y.; Iguchi, S.; Hagiwara, M. Feasibility study on plastic laser sintering without powder bed preheating. In Proceedings of the 22nd Annual International Solid Freeform Fabrication Symposium—An Additive Manufacturing Conference, SFF, Austin, TX, USA, 8–10 August 2011; 2011; 2011, pp. 17–29.
8. Niino, T.; Haraguchi, H.; Itagaki, Y.; Hara, K.; Morita, S. Microstructural observation and mechanical property evaluation of plastic parts obtained by preheat free laser sintering. In Proceedings of the 2012 International Solid Freeform Fabrication Symposium, Austin, TX, USA, 6–8 August 2012; University of Texas at Austin: Austin, TX, USA, 2012; pp. 617–628.
9. Kigure, T.; Yamauchi, Y.; Niino, T. Relationship between powder bed temperature and microstructure of laser sintered PA12 parts. In Proceedings of the 2019 International Solid Freeform Fabrication Symposium, Austin, TX, USA, 12–14 August 2019; University of Texas at Austin: Austin, TX, USA.
10. Zhang, D.; Zhang, P.; Liu, Z.; Feng, Z.; Wang, C.; Guo, Y. Thermofluid field of molten pool and its effects during selective laser melting (SLM) of Inconel 718 alloy. *Addit. Manuf.* **2018**, *21*, 567–578. [[CrossRef](#)]
11. Greiner, S.; Wudy, K.; Wörz, A.; Drummer, D. Thermographic investigation of laser-induced temperature fields in selective laser beam melting of polymers. *Opt. Laser Technol.* **2019**, *109*, 569–576. [[CrossRef](#)]
12. Drummer, D.; Greiner, S.; Zhao, M.; Wudy, K. A novel approach for understanding laser sintering of polymers. *Addit. Manuf.* **2019**, *27*, 379–388. [[CrossRef](#)]
13. Soldner, D.; Greiner, S.; Burkhardt, C.; Drummer, D.; Steinmann, P.; Mergheim, J. Numerical and experimental investigation of the isothermal assumption in selective laser sintering of PA12. *Addit. Manuf.* **2020**, *37*, 101676. [[CrossRef](#)]
14. Soldner, D.; Steinmann, P.; Mergheim, J. Modeling crystallization kinetics for selective laser sintering of polyamide 12. *GAMM-Mitteilungen* **2021**, *44*, e202100011. [[CrossRef](#)]
15. Bian, P.; Shao, X.; Du, J. Finite Element Analysis of Thermal Stress and Thermal Deformation in Typical Part during SLM. *Appl. Sci.* **2019**, *9*, 2231. [[CrossRef](#)]
16. Soe, S.P. Quantitative analysis on SLS part curling using EOS P700 machine. *J. Mater. Process. Technol.* **2012**, *212*, 2433–2442. [[CrossRef](#)]
17. Verbelen, L.; Dadbakhsh, S.; Van den Eynde, M.; Kruth, J.-P.; Goderis, B.; Van Puyvelde, P. Characterization of polyamide powders for determination of laser sintering processability. *Eur. Polym. J.* **2016**, *75*, 163–174. [[CrossRef](#)]
18. Santis, F.D.; Pantani, R.; Speranza, V.; Titomanlio, G. Analysis of Shrinkage Development of a Semicrystalline Polymer during Injection Molding. *Ind. Eng. Chem. Res.* **2010**, *49*, 2469–2476. [[CrossRef](#)]
19. Wegner, A.; Witt, G. Process monitoring in laser sintering using thermal imaging. In Proceedings of the 2011 International Solid Freeform Fabrication Symposium, University of Texas at Austin, Austin, TX, USA, 8–10 August 2011.
20. Jain, P.K.; Pandey, P.M.; Rao, P.V.M. Effect of delay time on part strength in selective laser sintering. *Int. J. Adv. Manuf. Technol.* **2008**, *43*, 117. [[CrossRef](#)]
21. Drexler, M.; Lexow, M.; Drummer, D. Selective Laser Melting of Polymer Powder—Part Mechanics as Function of Exposure Speed. *Phys. Procedia* **2015**, *78*, 328–336. [[CrossRef](#)]
22. Sindinger, S.-L.; Kralovec, C.; Tasch, D.; Schagerl, M. Thickness dependent anisotropy of mechanical properties and inhomogeneous porosity characteristics in laser-sintered polyamide 12 specimens. *Addit. Manuf.* **2020**, *33*, 101141. [[CrossRef](#)]
23. Pavan, M.; Faes, M.; Strobbe, D.; Van Hooreweder, B.; Craeghs, T.; Moens, D.; Dewulf, W. On the influence of inter-layer time and energy density on selected critical-to-quality properties of PA12 parts produced via laser sintering. *Polym. Test.* **2017**, *61*, 386–395. [[CrossRef](#)]
24. Schlicht, S.; Jaksch, A.; Drummer, D. Inline Quality Control through Optical Deep Learning-Based Porosity Determination for Powder Bed Fusion of Polymers. *Polymers* **2022**, *14*, 885. [[CrossRef](#)]
25. Paolucci, F.; Baeten, D.; Roozmond, P.C.; Goderis, B.; Peters, G.W.M. Quantification of isothermal crystallization of polyamide 12: Modelling of crystallization kinetics and phase composition. *Polymer* **2018**, *155*, 187–198. [[CrossRef](#)]
26. Lv, Y.; Thomas, W.; Chalk, R.; Hewitt, A.; Singamneni, S. Experimental Evaluation of Polyphenylsulfone (PPSF) Powders as Fire-Retardant Materials for Processing by Selective Laser Sintering. *Polymers* **2021**, *13*, 2704. [[CrossRef](#)] [[PubMed](#)]
27. Chatham, C.A.; Long, T.E.; Williams, C.B. Powder bed fusion of poly(phenylene sulfide) at bed temperatures significantly below melting. *Addit. Manuf.* **2019**, *28*, 506–516. [[CrossRef](#)]
28. Mubarak, Y.; Harkin-Jones, E.M.A.; Martin, P.J.; Ahmad, M. Modeling of non-isothermal crystallization kinetics of isotactic polypropylene. *Polymer* **2001**, *42*, 3171–3182. [[CrossRef](#)]
29. Piccarolo, S.; Saiu, M.; Brucato, V.; Titomanlio, G. Crystallization of polymer melts under fast cooling. II. High-purity iPP. *J. Appl. Polym. Sci.* **1992**, *46*, 625–634. [[CrossRef](#)]

30. Caldas, V.; Brown, G.R.; Nohr, R.S.; MacDonald, J.G.; Raboin, L.E. The structure of the mesomorphic phase of quenched isotactic polypropylene. *Polymer* **1994**, *35*, 899–907. [\[CrossRef\]](#)
31. Schael, G.W. A study of the morphology and physical properties of polypropylene films. *J. Appl. Polym. Sci.* **1966**, *10*, 901–915. [\[CrossRef\]](#)
32. Kapur, S.; Rogers, C.E. Aging of quenched polypropylene. *J. Polym. Sci. Polym. Phys. Ed.* **1972**, *10*, 2107–2124. [\[CrossRef\]](#)
33. Gezovich, D.M.; Geil, P.H. Morphology of quenched polypropylene. *Polym. Eng. Sci.* **1968**, *8*, 202–209. [\[CrossRef\]](#)
34. De Rosa, C.; Auriemma, F.; Di Girolamo, R.; de Ballesteros, O.R. Crystallization of the mesomorphic form and control of the molecular structure for tailoring the mechanical properties of isotactic polypropylene. *J. Polym. Sci. Part B Polym. Phys.* **2014**, *52*, 677–699. [\[CrossRef\]](#)
35. De Rosa, C.; Di Girolamo, R.; De Ballesteros, O.R.; Pepe, M.; Tarallo, O.; Malafronte, A. Morphology and Mechanical Properties of the Mesomorphic Form of Isotactic Polypropylene in Stereodeficient Polypropylene. *Macromolecules* **2013**, *46*, 5202–5214. [\[CrossRef\]](#)
36. Wang, D.; Yang, Y.Q.; Su, X.B.; Chen, Y.H. Study on energy input and its influences on single-track, multi-track, and multi-layer in SLM. *Int. J. Adv. Manuf. Technol.* **2012**, *58*, 1189–1199. [\[CrossRef\]](#)
37. Li, Z.; Xu, R.; Zhang, Z.; Kucukkoc, I. The influence of scan length on fabricating thin-walled components in selective laser melting. *Int. J. Mach. Tools Manuf.* **2018**, *126*, 1–12. [\[CrossRef\]](#)
38. Lu, Y.; Wu, S.; Gan, Y.; Huang, T.; Yang, C.; Junjie, L.; Lin, J. Study on the microstructure, mechanical property and residual stress of SLM Inconel-718 alloy manufactured by differing island scanning strategy. *Opt. Laser Technol.* **2015**, *75*, 197–206. [\[CrossRef\]](#)
39. Parry, L.; Ashcroft, I.A.; Wildman, R.D. Understanding the effect of laser scan strategy on residual stress in selective laser melting through thermo-mechanical simulation. *Addit. Manuf.* **2016**, *12*, 1–15. [\[CrossRef\]](#)
40. Catchpole-Smith, S.; Aboulkhair, N.; Parry, L.; Tuck, C.; Ashcroft, I.A.; Clare, A. Fractal scan strategies for selective laser melting of ‘unweldable’ nickel superalloys. *Addit. Manuf.* **2017**, *15*, 113–122. [\[CrossRef\]](#)
41. Greiner, S.; Schlicht, S.; Drummer, D. Temperature field homogenization by fractal exposure strategies in laser sintering of polymers. In Proceedings of the 17th Rapid.Tech 3D Conference, Erfurt, Germany, 22–23 June 2021; Carl Hanser Verlag GmbH & Co. KG: Munich, Germany, 2021; pp. 188–197, ISBN 978-3-446-47171-9.
42. Bader, M.; Bungartz, H.-J.; Mehl, M. Space-Filling Curves. In *Encyclopedia of Parallel Computing*; Padua, D., Ed.; Springer: Boston, MA, USA, 2011; pp. 1862–1867. ISBN 978-0-387-09766-4.
43. Peano, G. Sur une courbe, qui remplit toute une aire plane. *Math. Ann.* **1890**, *36*, 157–160. [\[CrossRef\]](#)
44. DIN EN ISO 1628-3:2010-10; Kunststoffe—Bestimmung der Viskosität von Polymeren in verdünnter Lösung durch ein Kapillarviskosimeter—Teil 3: Polyethylen und Polypropylen. Beuth Verlag GmbH: Berlin, Germany, 2010. [\[CrossRef\]](#)
45. Shen, F.; Zhu, W.; Zhou, K.; Ke, L.-L. Modeling the temperature, crystallization, and residual stress for selective laser sintering of polymeric powder. *Acta Mech.* **2021**, *232*, 3635–3653. [\[CrossRef\]](#)
46. Osmanlic, F.; Wudy, K.; Laumer, T.; Schmidt, M.; Drummer, D.; Körner, C. Modeling of Laser Beam Absorption in a Polymer Powder Bed. *Polymers* **2018**, *10*, 784. [\[CrossRef\]](#)
47. Mileva, D.; Wang, J.; Gahleitner, M.; Jariyavidyanont, K.; Androsch, R. New Insights into Crystallization of Heterophasic Isotactic Polypropylene by Fast Scanning Chip Calorimetry. *Polymers* **2020**, *12*, 1683. [\[CrossRef\]](#)

Disclaimer/Publisher’s Note: The statements, opinions and data contained in all publications are solely those of the individual author(s) and contributor(s) and not of MDPI and/or the editor(s). MDPI and/or the editor(s) disclaim responsibility for any injury to people or property resulting from any ideas, methods, instructions or products referred to in the content.